

Title:

Optical clearing of living brains with MAGICAL to extend *in vivo* imaging

Authors:

Kouichirou Iijima¹, Takuto Oshima², Ryosuke Kawakami^{1,2}, Tomomi Nemoto^{1,2*}

Affiliations:

1 Research Institute for Electronic Science, Hokkaido University, N20W10, Kita-ku, Sapporo,
Hokkaido 001-0020, Japan.

2 Graduate School of Information Science and Technology, Hokkaido University, N14W9, Kita-ku,
Sapporo, Hokkaido 060-0814, Japan.

* Corresponding author. Email: tn@es.hokudai.ac.jp

14 **Abstract:**

15 To understand brain functions, it is important to observe directly how multiple neural circuits are
 16 performing in living brains. However, due to tissue opaqueness, observable depth and
 17 spatiotemporal resolution are severely degraded *in vivo*. Here, we propose an optical brain clearing
 18 method for *in vivo* fluorescence microscopy, termed MAGICAL (Magical Additive Glycerol
 19 Improves Clear Alive Luminance). MAGICAL enabled two-photon microscopy to capture vivid
 20 images with fast speed, at cortical layer V and hippocampal CA1 *in vivo*. Moreover, MAGICAL
 21 promoted conventional confocal microscopy to visualize finer neuronal structures including
 22 synaptic boutons and spines in unprecedented deep regions, without intensive illumination leading
 23 to phototoxic effects. Fluorescence Emission Spectrum Transmissive Analysis (FESTA) showed
 24 that MAGICAL improved *in vivo* transmittance of shorter wavelength light, which is vulnerable to
 25 optical scattering thus unsuited for *in vivo* microscopy. These results suggest that MAGICAL
 26 would transparentize living brains via scattering reduction.

27

28

29 Main Text:

30 How do neurons work together for brain functions in living animals? In the brain, numerous
 31 neurons connect to each other three-dimensionally (3D) to form neural circuits underlying brain
 32 functions. Functional characteristics of neural circuits depend on neuronal activity and synaptic
 33 connectivity, both of which are reflected in fine sculptural distinctions in many cases¹⁻³. Multiple
 34 neural circuits are associated with each other as a neural network, and are executed for rapid
 35 processing simultaneously, to respond to various situations and their transitions⁴. Therefore, to
 36 understand brain functions, *in vivo* imaging techniques are required to observe intact neural circuits
 37 extended into deep regions, at high spatiotemporal resolution.

38 Confocal microscopy and two-photon microscopy can provide 3D and time-lapse images by
 39 sequential optical sectioning in thick specimens without mechanical destruction^{5,6}. However, it is
 40 difficult for the fluorescence microscopy, especially to confocal microscopy, to achieve sufficiently
 41 deep, fine, and fast imaging *in vivo*, because tissue opaqueness disturbs and attenuates both
 42 excitation lights and fluorescence signals. A simple but practical technique to overcome the
 43 opaqueness is high-intensity illumination by using high-power excitation laser, but it has a risk of
 44 causing invasive phototoxic problems via reactive oxygen species production. Thus, new strategies
 45 are needed to overcome tissue opaqueness for *in vivo* imaging.

46 Recently, many optical clearing methods were reported for fluorescence microscopy in fixed
 47 organs including brains⁷⁻¹³. These clearing methods enable confocal microscopy to achieve fine and
 48 deeper imaging, and have brought a paradigm shift in connectome analysis, to create connection
 49 maps over comprehensive neural networks. However, these clearing methods need
 50 non-physiological procedures to transparentize fixed organs, thus are especially inapplicable to
 51 living brains for *in vivo* fluorescence microscopy. Here, we propose a new strategy for
 52 brain-clearing in *in vivo* microscopy. Our clearing method is simply based on glycerol
 53 administration via drinking water, so we named it MAGICAL (Magical Additive Glycerol
 54 Improves Clear Alive Luminance).

Results:

Enhanced fluorescence signals *in vivo*.

For *in vivo* brain imaging with fluorescence microscopy, the conventional method involves open-skull surgery. It consists of making a cranial window, in which the light-scattering skull bone is replaced by a clear cover glass, and is conceived as a key step affecting the quality of images in day-to-day experiments¹⁴. The cranial window, and probably the brain itself, lose transparency easily, which may be caused by unsuitable surgical techniques, leading to bleeding and damage inside/outside the brain, and by unknown factors related with the recovery process. Thus, a smaller cranial window is biologically preferred to avoid injuring blood vessels and to minimize contact between the brain surface and the surgical materials¹⁴. However, a larger cranial window is optically preferred to collect even light emitted from a focal point at wide radiation angles, by using a high-numerical-aperture (NA) lens which governs spatial resolution and fluorescence intensity in imaging. Therefore, we tried to improve *in vivo* microscopy by reducing the detrimental effects of open-skull surgery. We focused on glycerol oral administration, which is known to suppress cerebral edema in neurosurgical patients and suggested to supply energy to ischemic neurons in cerebral stroke¹⁵⁻²².

First, we examined whether oral administration of glycerol improves cerebral fluorescence images of *in vivo* two-photon microscopy. To visualize neural circuits, we used adult H-line mice (Thy1-EYFP-H), which express Enhanced Yellow Fluorescent Protein (EYFP) in some of the pyramidal neurons. To avoid selection bias under uneven EYFP expression, the imaging area was selected according to the xy position where the hippocampus was observable at the most shallow depth. We captured 3D stacks as z-series of xy-images, using a two-photon microscope with 960-nm Ti:Sapphire laser light. The xy-images were acquired as 512×512 pixels at 1 frame per sec (fps), 2.2 μ sec per pixel, which is the maximum speed in this condition.

The images of the cortical layer V (CxLV) neurons were captured with 3- μ m z-step size (**Supplementary Movie 1**) and were reconstructed with depth color-coded maximum intensity

projection (DccMIP). In mice without glycerol administration (control), fluorescence images showed the pyramidal neuron cell bodies with basal dendrites, but the density was poor as a consequence of weak capture conditions (**Fig. 1a, Supplementary Movie 1**). In contrast, in mice with 5 % (w/v) glycerol administration (MAGICAL), bright fluorescence images showed many cell bodies and basal dendrites with high density (**Fig. 1a, Supplementary Movie 1**).

In CxLV images at three different depths (**Supplementary Fig. 1**), fluorescence intensity distribution (FID) indicated that signals tended to increase with MAGICAL (**Supplementary Fig. 2**). However, it was not simple to summarize the FIDs for statistical analysis. The FIDs showed large individual differences within each treatment group, obscuring differences between the groups. Moreover, the FIDs had non-normal distributions extending beyond the detector's dynamic range. To overcome these problems, we evaluated fluorescence intensities of pixels (FIPs) in the image stacks, by using a Generalized Linear Mixed Model (GLMM). The FIPs were randomly selected from the stack and collected as samples, if not saturation or zero intensity, and were used as a response variable in the GLMM with a Gamma error distribution and a log link function. In the GLMM, "Treatment" (MAGICAL or control) and "Depth" (3 levels) were assigned as fixed effects, and "Mouse" was assigned as a random effect for intercepts and "Depth" slopes. The GLMM comprised 929,331 FIPs in 78 image stacks, extracted from 3 depths of 26 mice under 2 treatments ($R^2_{GLMM(m)}: 0.0147$, $R^2_{GLMM(c)}: 0.200$, **Supplementary Table 1a**). In estimation for fixed effects, the GLMM indicated that MAGICAL enhanced FIPs in the CxLV images (**Fig. 1b–c**; $p < 0.001$ at each "Depth" level by pairwise comparison). These signal enhancements mean that MAGICAL can overcome tissue opaqueness enough to improve *in vivo* imaging.

***In vivo* two-photon deep imaging with fast speed.**

To achieve *in vivo* imaging in deeper regions, the most effective strategy is to use much longer-wavelength, less scattered, near-infrared light at high power for two-photon excitation^{23,24}. Recently, hippocampal granule cells in the dentate gyrus were visualized at 1.5-mm depth in adult mice by using a 1064 nm laser-diode light, in the most successful surgery without bleeding²⁴.

Furthermore, hippocampal CA1 (HpCA1) neurons can be visualized at 1.0-mm depth in adult mice, by using 1000 nm Ti:Sapphire laser light²⁴. However, despite the advantage of longer-wavelength strategy, fluorescence acquisitions must collect shorter visible light, attenuated more easily by scattering and absorption in tissues depending on return distance. Indeed, both deep imaging techniques require scanning neurons at 1/16 or less fps, which is extremely slow, to visualize neural activity and to overcome image distortions caused by heartbeats. So, as a touchstone of *in vivo* deep imaging, we examined whether MAGICAL improves adult HpCA1 images at fast scanning.

By using 960 nm Ti:Sapphire laser light, HpCA1 images approximately at 1.0-mm depth were captured as 3D stacks, having xy-images (512×512 pixels) with 1 fps fast speed. In control mice, fluorescence images showed some dim cell bodies of pyramidal neurons (**Fig. 2a, Supplementary Fig. 3**). In contrast, in MAGICAL mice, fluorescence images showed many cell bodies of pyramidal neurons, some of which were clearly visualized with their partial process of apical dendrite (**Fig. 2a, Supplementary Fig. 3**).

In HpCA1 images captured from three different depths $\pm 3 \mu\text{m}$ (**Supplementary Fig. 4**), FIDs were shifted to bright side with MAGICAL (**Supplementary Fig. 5**). GLMM at HpCA1 was comprised with 957,264 FIPs in 78 image stacks extracted 3 depths from 26 mice under 2 treatments ($R^2_{GLMM(m)}$: 0.0714, $R^2_{GLMM(c)}$: 0.190, **Supplementary Table 1b**). In estimation for fixed effects, the GLMM indicated that MAGICAL also enhanced FIPs in the HpCA1 images, despite long traversing from deep regions (**Fig. 2b–c**; $p < 0.001$ at each “Depth” level by pairwise comparison). These results suggest that MAGICAL would promote deep imaging as a practical method to visualize fast activity on mature neural circuits in adult mice.

***In vivo* confocal fine imaging with single-photon excitation at deeper regions.**

Despite its superior spatial resolution, confocal microscopy is less suitable for *in vivo* imaging than two-photon microscopy, because its shorter-wavelength excitation has an inferior penetration depth and a higher risk for phototoxic effects. Moreover, confocal microscopy cannot efficiently

collect fluorescence signals due to a confocal aperture, which excludes most of the signals scattered by the tissue but is needed to remove extrafocal light causing image blur. Therefore, confocal microscopy is vulnerable to tissue opaqueness, especially optical scattering. In general, *in vivo* confocal microscopy is hardly able to visualize fine neural fibers below 50- μ m depth, which poses a dilemma between clear visualization and phototoxicity reduction²⁵. The abovementioned effects of MAGICAL on *in vivo* two-photon imaging, suggest that it may overcome that dilemma.

Thus, we examined to what extent MAGICAL enables *in vivo* confocal microscopy to visualize neural fibers at deeper regions. We captured 3D stack images of cortical layer I (CxLI) at 50 ± 5 , 100 ± 5 , and 150 ± 5 μ m depth in H-line mice, by using a confocal microscope with 488-nm laser light (CM image) and a two-photon microscope with 960-nm (2PM image as a reference). The 3D stack images comprise 1- μ m-step z-series of xy-images, acquired as 512×512 pixels at 1 fps. In control mice, dim CM images at 100 and 150 μ m depth were hardly able to visualize fine neural fibers except for thick shafts of apical dendrites which extend along the z-axis direction (**Fig. 3a**, **Supplementary Fig. 6**). However, in MAGICAL mice, bright CM images even at 100 and 150 μ m depth showed a lot of thin neuronal processes extending in the xy-plane across the apical dendrite shaft (**Fig. 3a**, **Supplementary Fig. 6**).

We quantified similarities between CM images and 2PM reference images at same CxLI areas, by using the intersection probability between Histogram of Oriented Gradients (HOG) features extracted from each image. In the HOG comparison, CM images with MAGICAL retained more similarity to 2PM reference images at deeper regions (**Fig. 3b–d**, $p = 0.0484$ at 100 μ m depth, $p = 0.0420$ at 150 μ m depth, in permuted Brunner-Munzel test, $n = 6$ in control mice, $n = 7$ in MAGICAL mice). These results show that MAGICAL improves the observable depth at which *in vivo* confocal imaging can visualize detailed features.

To evaluate visualization abilities of confocal microscopy with MAGICAL, we captured 3D stack images with high-magnification at around 100 μ m depth. In MAGICAL mice, the images showed synaptic structures, such as dendritic spines and axonal boutons, clearly, and fine fibers with less optical aberration along the z-axis (**Fig. 4**, **Supplementary Fig. 7**). Moreover, *in vivo*

confocal images with MAGICAL did not show remarkable bleaching or phototoxic effects, as observed in time-lapse 3D stack imaging at 5-min intervals for 30 min (**Fig. 4, Supplementary Fig. 7**). These data suggest that MAGICAL would provide a practical approach to observe deeper regions with superior spatial resolution beyond the dilemma posed by confocal microscopy.

Evaluation of clearing ability by FESTA.

Fluorescence signal enhancement at several depths is one of the phenomena expected with optical clearing. However, it remains unclear whether MAGICAL improves transparency inside living brains. To address the question, we tried to evaluate *in vivo* transmittance at different wavelengths through the brain.

In conventional transmissive analyses, a certified light source is needed on the other side of a detector beyond a target, to calculate transmittance, i.e., the intensity ratio of transmissive light through a target to incident light from the source. In this perspective, fluorescence probes do not suit the light source for *in vivo* transmissive analysis, because original fluorescence intensity within focal point depends on the amount of the fluorescence probes and intensity of transmitted excitation light, both of which are unknown and uncontrollable inside living brains. However, a fluorescence emission spectrum is physically certified as emission probability at wavelengths, determined by energy levels and transition frequencies inherent in its molecule. Thus, to evaluate *in vivo* transmittance, we developed a new analytical method, Fluorescence Emission Spectrum Transmissive Analysis (FESTA), by using the emission spectrum as a scale independent of whole fluorescence intensity.

As fluorescence resources of *in vivo* FESTA, artificial yellow-green (YG) beads (Fluoresbrite YG Microspheres, Calibration Grade 1 μm ; Polysciences) were injected into living mouse brains, and then were scattered in small clusters with cerebrospinal fluid flow. We calculated spectral intensity ratio of Cyan (458–511 nm) to Yellow (560–650 nm) light within *in vivo* images of the bead clusters (**Fig. 5a**). In contrast to fluorescence intensity, the Cyan/Yellow ratio was independent on both of amount of the fluorescence probes and two-photon excitation power

(Supplementary Fig. 8). However, the Cyan/Yellow ratio was different between depths (Supplementary Fig. 8). Therefore, it is considered that the Cyan/Yellow ratio is proportional to a ratio, comprising the emission probability (constant), detector sensitivity (fixed as constant), and transmittance in the return path from inside the brain, for the Cyan and Yellow light.

To focus on internal transmittance in living brains, and to remove the constant factors, we evaluated spectral transmission ratio ($\Delta\text{Cyan/Yellow}$) while the light returned from deeper regions to 100 μm depth. The $\Delta\text{Cyan/Yellow}$ gradually decreased along the depth (Fig. 5b). It is, therefore, reasonable to consider that the cyan transmittance is more likely to be decreased than the yellow one because shorter wavelength light is more scattered depending on the optical path-length. However, in MAGICAL, a decrease of $\Delta\text{Cyan/Yellow}$ was suppressed at deeper regions ($p = 0.00159$ in unpaired two-tailed Welch's t -test, 95 % confidence interval (CI) = 0.0551–0.174, $t = 4.29$, $df = 10.0$, Cohen's $d = 2.48$, $n = 6$ mice in each group, at 600 μm depth). These results suggest that MAGICAL improves *in vivo* transmittance especially of shorter wavelength light susceptible to optical scattering. Thus, we conclude that MAGICAL exerts an optical clearing ability to reduce scattering in living brains.

Discussion:

MAGICAL improved clear fluorescence signals, which would be enough to achieve faster imaging at deeper regions, *in vivo*. The imaging speed is one of the most important factors for *in vivo* observation. Fast imaging enables the visualization of not only instantaneous changes in neural activity with high temporal resolution but also finer structures of neural circuits by overcoming heartbeat-related trembles. In addition, fast imaging is required for enhancement of spatial resolution per time unit and expansion of observable areas within limited experimental time. Furthermore, fast imaging would be preferred to reduce phototoxic effects *in vivo*. Thus, MAGICAL would be a fundamental method for *in vivo* imaging to observe extensive neural circuits at high spatiotemporal resolution with less invasiveness.

Our results suggested that MAGICAL can transparentize living brains via scattering reduction.

This leads us to the question of how does MAGICAL suppress the optical scattering in living brains? Generally, the major source of optical scattering in tissues is refractive index mismatches between structural components (n_d ; approx. 1.5) and interstitial fluids (water, n_d ; 1.33). A conventional optical clearing is achieved by increasing the refractive index of fluids with high index reagents, including glycerol (n_d ; 1.47 at 100 %), which can infiltrate into tissues and/or replace original fluids by itself, and as a result, reduce the mismatches. This clearing approach is useful for *in vivo* imaging to penetrate into tough tissues, such as skin²⁶ and skull²⁷, where glycerol immersion is tolerable even at high concentration keeping a high refractive index. However, glycerol also causes hemolysis *in vivo* as a function of dose, concentration, and route of administration^{15,28}, indicating that the conventional technique using higher concentration glycerol is less applicable for almost *in vivo* tissues. Moreover, MAGICAL achieves optical clearing of living brains regardless of low concentration glycerol (5 %), which has almost the same refractive index as water. Therefore, to explain optical clearing by MAGICAL, other mechanisms different from conventional ones are needed.

MAGICAL was designed in reference to the medical treatment for cerebral edema and ischemic stroke¹⁵⁻²¹. Cerebral edema may occur for various reasons: cerebral trauma and inflammation allow the leak of serum proteins, drawing fluid into the brain due to the breakdown of the blood-brain barrier²⁹. Furthermore, ischemia and hypoxia cause cell swelling due to a dysfunction of ion pumps caused by energy depletion²⁹. The cerebral edema, in turn, reduces blood flow (ischemia) as a consequence of intracranial hypertension, thereby deteriorating hypoxia. Clinically, glycerol is commonly administrated to neurosurgery and stroke patients, in order to reduce edema via dehydration, thus to decrease intracranial pressure (ICP), and to increase cerebral blood flow^{16,17,19-21}. From an optical point of view, light scattering is increased in living brains under cerebral ischemia and hypoxia, experimentally induced by blood removal and nitrogen gas inhalation, respectively^{30,31}. The increased scattering is attributed to disturbances in cellular/subcellular structures due to the energy depletion. In the case of *in vivo* microscopy, living

245 brains are exposed to loads, such as open-skull surgery, illumination for fluorescence excitation,
246 and slight hypoxia from anesthesia. These loads cause brain trauma and inflammation, which in
247 turn would trigger local edema, which, although not as severe as experimental ischemia and
248 hypoxia, is enough to increase scattering for shorter wavelength light. Altogether, MAGICAL
249 protects the living brains from edema and ischemia and thus would preserve the brain transparency.

250 What are the adverse effects of using MAGICAL for *in vivo* imaging? In toxicity tests, chronic
251 oral glycerol has been shown as safe for animals, when administered in dosages equal to or lower
252 than 9 g/kg-bw/day^{32,33}. Thus, MAGICAL is considered as a non-invasive treatment, considering
253 that 4.5-ml of 5 % (w/v) glycerol is daily administered as drinking water to a mouse weighing
254 approximately 25-g. In the treatment of cerebral edema, glycerol administration does not show
255 severe ICP rebound, electrolyte imbalance, and toxic side effects^{16,17,20,21}. In addition, glycerol
256 administration is expected to improve electroencephalogram and neurological status in ischemic
257 stroke patients¹⁷⁻¹⁹. Moreover, glycerol administration is also commonly used to reduce intraocular
258 pressure in glaucoma patients, without significant side effects suggestive of neurologic
259 dysfunction³⁴. These results suggest that MAGICAL would less disturb fundamental mechanisms
260 executing brain functions. However, glycerol administration would improve energy metabolism in
261 ischemic brains¹⁹, indicating that glycerol can be a cue to trigger some neural activity. The extent to
262 which MAGICAL can modulate neural activity remains unclear, and thus probably should be
263 evaluated for each neural circuit of interest.

264 MAGICAL is the first candidate for the optical clearing method applicable to living brains,
265 easily improving *in vivo* microscopy without requiring any special skills or devices. Improved
266 transparency for shorter-wavelength light with MAGICAL, means to expand the usability of
267 various light sources, luminous probes, photosensitive caged compounds, and optogenetic tools for
268 *in vivo* imaging and optical manipulation. In other words, MAGICAL is an important contribution
269 toward for scientific advance, requiring a multi-laser/probe combination, such as the stimulated
270 emission depletion microscopy³⁵, photo-stimulation techniques³⁶, and multi-color imaging³⁷.
271 Moreover, MAGICAL enables *in vivo* microscopy via the cranial window, to be combined with

272 other neurological methods that insert electrodes or glass capillaries. These classical methods have
273 been less compatible with *in vivo* microscopy due to an open-skull dogma that prohibits from
274 contacting the brain for clear imaging. However, MAGICAL's clearing ability has been
275 demonstrated, despite after artificial beads injections in the FESTA. Thus, MAGICAL would
276 accelerate functional analysis for brain functions, only by oral administration of glycerol.
277

278 **Methods:**

279

280 No statistical methods were used to predetermine sample size. In Generalized Linear Mixed
281 Models (GLMMs), we used large sample sizes generally enough for modeling. For the Welch's
282 *t*-test, we confirmed that the *t*-test had adequate power, with a post-hoc test having effect size
283 (Cohen's *d*), *p*-value (< 0.01), and the sample size.

284 The experiments were not randomized. *In vivo* imaging must observe individual mice convergently,
285 not parallelly, for a long time. To reduce influence dependent on specific timing, the observation
286 order for each experimental group should be uniformly mixed. However, the sample size is
287 insufficient for randomization to ensure to equalize the order. Thus, we allocated mice to
288 experimental groups so as not to localize the order.

289 Investigators were not blinded to allocation during experiments and data analysis. To remove
290 observer bias during experiments, observation area was selected by previously defined criteria, as
291 described in "Methods, 'Fluorescence intensity analysis' section". Data collection and analysis were
292 automatically performed by software with fixed parameter setting or macro programs.

293

294 **Animals.** All experiments were conducted in accordance with the Animal Research Committee of
295 the Hokkaido University. The protocols were approved by the Committee on the Ethics of Animal
296 Experiments in the Hokkaido University (No. 10-0119). Adult transgenic mice (9 to 12 weeks old,
297 male) from Thy1-EYFP-H (H-line) were used for *in vivo* imaging of neurons. Adult
298 C57BL/6NCrSlc mice (10 to 22 weeks old, male; Japan SLC, Shizuoka, Japan) were used for the
299 FESTA with injected fluorescent beads. All mice were housed with food and drink *ad libitum* and
300 were maintained in a 12 h light-dark cycle (lights on from 8:00 to 20:00), with controlled
301 temperature (22 °C to 26 °C) and humidity (40 % to 60 %).

302

303 **Glycerol administration.** For MAGICAL mice, 5 % (w/v) glycerol (075-00616; Wako Pure
304 Chemical Industries, Osaka, Japan) was administered orally in the drinking water, *ad libitum*, from

2 weeks prior to open-skull surgery to the end of the experiment, except during operations and observations. Control mice received only water.

Open-skull surgery. A cranial window was surgically created overlying the left cortex, according to a previous protocol^{14,23}, with minor modifications. Briefly, 45 mg/kg-bw minocycline (Nichi-Iko Pharmaceutical, Toyama, Japan) were injected intraperitoneally (i.p.) about 4 h before surgery, to suppress bacterial infection and to protect neurons against microglial activation (neuroinflammation). Anesthesia was induced with an i.p. injection of 60 mg/kg-bw pentobarbital sodium (Somnopentyl; Kyoritsu Seiyaku Corporation, Tokyo, Japan), and was maintained with isoflurane inhalation (0.5 % to 1.5 %). To limit inflammation, 2 mg/kg-bw dexamethasone (Kyoritsu Seiyaku Corporation) was injected intramuscularly. Cranial bones were exposed, and then the left parietal bone was circularly carved about 4.2 mm in diameter with a dental drill and was removed gently. The exposed dura was washed with phosphate-buffered saline (PBS) to remove blood cells. A 4.2-mm diameter round coverslip (Micro Cover GLASS, #1S, about 0.17 mm thickness; Matsunami Glass Industry, Osaka, Japan), previously coated with a biocompatible polymer—Lipidure® (CM5206E; NOF Corporation, Tokyo, Japan), to prevent foreign-body reactions, especially to blood clotting—was placed directly over the dura without extra pressure, and was sealed on the bone edges with cyanoacrylate cement and dental adhesive resin cement (Super-Bond C&B; Sun Medical Company, Shiga, Japan). To make the foundations for chamber fixation, exposed cranial bones around the cranial window were partially coated with the adhesive resin cement. A head chamber, which has a center hole to expose the cranial window, was secured to the cranial bones with dental acrylic resin cement (Unifast III; GC Corporation, Tokyo, Japan). 5 mg/kg-bw carprofen (Rimadyl; Zoetis, Parsippany, NJ, USA) was injected i.p. to reduce inflammation and pain. After surgery, the mouse was singly housed for recovery at least 3 hours until observation.

331 **Beads injection.** The beads injection into the cortex was performed in an open-skull surgery, with
 332 minor modifications before sealing with the coverslip, by using an oil filled glass micropipette
 333 attached to a mechanically driven Hamilton microsyringe. The left parietal bone was elliptically
 334 resected about 3.9-mm in the anterior-posterior (A-P) axis and about 2.7-mm in the medial-lateral
 335 axis. A needle of the glass micropipette was inserted into the cortex at an angle of 54 degrees with
 336 respect to the brain surface, and proceeded 0.9 mm towards the anterior direction along the A-P
 337 axis, to reach about 0.72 mm depth. 1- μ m YG beads (Fluoresbrite® YG Microspheres, Calibration
 338 Grade 1 μ m, #18860; Polysciences, Incorporated, Warrington, PA, USA) were diluted at 4.6×10^8
 339 beads/mL with PBS, and were gradually injected into the needle trace in repeated steps, in which
 340 the needle was withdrawn 0.3 mm and then was kept in place for 5 min. During and after the
 341 injection, the exposed dura was washed with PBS to remove blood cells and to prevent drying.
 342 After the surgery, the mouse was singly housed for recovery at least one day until observation.

343
 344 **Setup of *in vivo* imaging.** All *in vivo* imaging sessions were conducted in mice anesthetized with
 345 isoflurane inhalation^{23,24}. The head chamber was mounted and glued to a customized adaptor stage,
 346 which suspended the mouse body with a harness, to reduce adverse effects due to movements.
 347 After setting under an upright microscope system, the adaptor stage was adjusted at a tilt angle,
 348 referring to 1- μ m diameter fluorescent beads scattered on the coverslip as a guide, so that the
 349 cranial window was positioned horizontally, hence providing a suitable optical alignment. All *in*
 350 *vivo* imaging sessions were performed under a microscope system (A1R MP+ Multiphoton
 351 Confocal Microscope; Nikon, Tokyo, Japan) controlled by NIS-Elements software (version
 352 4.13.00; Nikon) with 12-bit dynamic range. Before *in vivo* imaging, z-position at the brain surface
 353 was set as zero for absolute depth.

354
 355 **Two-photon microscopy.** *In vivo* two-photon imaging was performed with a water immersion
 356 objective (25 \times Ob., 1.10 NA) in PBS. The EYFP and the YG beads were excited by 960 nm and
 357 900 nm, respectively, emitted from Ti:Sapphire laser (Mai Tai DeepSee; Newport Spectra-Physics,

Irvine, CA, USA). By using a Galvano scanner in one-directional mode, the xy-images in the 3D stacks were acquired as 512×512 pixels at 1 frame per sec (fps), 2.2 μ sec per pixel, which is maximum speed in this condition. The 3D display was performed using the NIS-Elements software.

To visualize the neural circuits, all the EYFP signals under 650-nm wavelength were collected in a GaAsP type Non-Descanned Detector (GaAsP-NDD). The CxLV and HpCA1 images were captured as 3D stacks with 3 μ m z-step size. The depth of the CxLV was determined between 495 μ m and 585 μ m, where somas of CxLV pyramidal neurons were observed in every mouse. The depth of the HpCA1 was slightly different for each mouse, thus the middle of stratum pyramidale, approximately at 975 μ m absolute depth, was set as the center depth of each HpCA1 stack. To evaluate the brightness of the images, laser power (LP) under objective lens and detector sensitivity (HV: high voltage) were fixed. The CxLV was captured with LP 66 mW (under 25 \times Ob.) and HV 30. The HpCA1 was captured with LP 200 mW (under 25 \times Ob.) and HV 30.

For the FESTA, fluorescence signals were split to multi-colors by dichroic mirrors (DM) in front of the GaAsP-NDDs. The signals of YG beads were split by DM458, DM511, and DM560, and then separately detected at 458–511 nm (Cyan) and at 560–650 nm (Yellow). To avoid optical influence by injection trace, the FESTA applied to the beads clusters observable without crossing the trace. The beads images were captured as 3D stacks with 0.25 μ m z-step size at depth of interest \pm 1.0 μ m (9 sections). The detector sensitivities were fixed: HV 1 on the Cyan channel and HV 3 on the Yellow channel. The laser powers were adjusted for each bead cluster, because bead clusters show different brightness depending on cluster size and injection depth.

Confocal microscopy. *In vivo* confocal imaging was performed with a water immersion objective (25 \times Ob., 1.10 NA or 60 \times Ob., 1.20 NA) in PBS. The EYFP was excited by 488 nm, and its signal was collected at 500–550 nm in a standard detector. By using a Galvano scanner in one-directional mode, the xy-images comprising 3D stacks were acquired as 512×512 pixels at 1 fps or 512×256 pixels at 2 fps, 2.2 μ sec per pixel, which is maximum speed in this condition.

385 To evaluate observable depth in confocal imaging, the CxLI images were captured as 3D stacks
 386 with 1 μm z-step size at 50 ± 5 , 100 ± 5 , and 150 ± 5 μm depth (11 sections) via a $25\times$ Ob. Laser
 387 power and detector sensitivity were fixed at 10 % and HV 90, respectively. As references for
 388 confocal imaging, the same 3D stacks were also captured by using a two-photon microscope, of
 389 which detector sensitivity was fixed at HV 30, but 960-nm laser powers were adjusted to 12.5, 16.1,
 390 and 19.2 mW (under $25\times$ Ob.) at 50, 100, and 150 μm depth, respectively.

391 High-resolution 4D imaging with a $60\times$ Ob. was performed as 3D stacks with 1 μm z-step size
 392 at approximate 100 ± 15 μm depth (31 sections), as a time-series at 5 minutes intervals for 30
 393 minutes (7 time-points). Laser power and detector sensitivity were set between 10 and 20 % and
 394 between HV 90 and HV 100, respectively. The 3D display was performed by NIS-Elements
 395 software.

396

397 **Fluorescence intensity analysis.** For two-photon imaging at CxLV and HpCA1, 30 mice
 398 (Treatment: control, $n = 15$; MAGICAL, $n = 15$) were observed. For confocal imaging at CxLI, 17
 399 mice (Treatment: control, $n = 8$; MAGICAL, $n = 9$) were observed. In the H-line mice, signal
 400 distribution is uneven, especially at the somatic layer, because the EYFP expression level varies
 401 among positive neurons, which tend to be differently clustered in different individuals. To avoid
 402 selection bias due to individual differences, the imaging area was selected according to the xy
 403 position where the hippocampus was observable at the most shallow depth.

404 Fluorescence intensity analysis was performed on the 3D image stacks, by using Fiji/ImageJ
 405 software (version 2.0.0-rc-49/1.51d)³⁸. For sorting of image stacks within each capture condition,
 406 mice were ranked in descending order of brightness (average fluorescence intensity per pixel)
 407 extracted from image stacks around the center region: at 540 ± 12 μm for the CxLV, approximately
 408 at 975 ± 12 μm for the HpCA1, and at 100 ± 5 μm for the CxLI. The top or bottom brightness at
 409 each capture condition came from over- or under-exposed image stacks, respectively. Thus, mice
 410 having the top or bottom brightness within each treatment group were equally removed from the
 411 following analysis, as outliers of the capture condition. Finally, 26 mice (control, $n = 13$;

MAGICAL, $n = 13$) and 13 mice (control, $n = 6$; MAGICAL, $n = 7$) were evaluated in fluorescence intensity analysis for two-photon imaging and confocal imaging, respectively. A representative image for each treatment group at each capture condition was obtained from the mouse scored as intermediate brightness.

In the two-photon imaging, we evaluated the fluorescence intensity distributions (FIDs) under HV 30, at three different depths within the observation area. For the CxLV, the three depths were set at 510 ± 3 , 540 ± 3 (center), and 570 ± 3 μm depth. For the HpCA1, three depths were relatively adjusted at the middle of stratum pyramidale as the center (0 μm), approximately at 975 ± 3 μm absolute depth, and at 24 μm above and below the center. These three depths were sufficiently far away from each other to ensure separate images in the mice.

The FIDs were summarized to 8-bit intensity bins histograms by the Fiji and were visualized through following steps by R (version 3.3.2)³⁹ with RStudio software (version 1.0.44). The histograms were arranged as a matrix, where the image stacks were sorted in rows according to their brightness in decreasing order, and the intensity bins were aligned in columns. Pixel counts (z) in the histogram were converted with $\log_{10}(z+1)$, where 1 is a constant to avoid $\log_{10}(0)$ contamination in the converted matrix. The matrix of FIDs was visualized as a heat map. Pixel counts (excluding zero) were ranked in percent quantile. In the heat maps, the 50 % quantile was shown as cyan dotted contours.

Image similarity analysis. Based on image features, similarities between CM images and 2PM reference images at same CxLI areas were evaluated in 13 mice (Treatment: control, $n = 6$; MAGICAL, $n = 7$), which passed fluorescence intensity analysis to remove outliers. The 3D stack images were converted to DccMIP 2D images with a color code shown in **Fig. 3a**, by using Fiji/ImageJ software. The display range of fluorescence intensity (min–max in 8 bits) were adjusted as follow: 2PM images at every depth, (0–127); CM images at 50, 100, and 150 μm depth, (0–255), (0–127), and (0–63), respectively.

438 Features extraction and comparison were performed by using OpenCV (version 3.4.2) via a
 439 python (version 3.6.6) code. In gray-scale space, a Histogram of Oriented Gradients (HOG)⁴⁰
 440 feature was extracted from each image (512×512 pixels) with parameters as follow: window size,
 441 (512, 512); block size, (128, 128); block stride, (4, 4); cell size, (16, 16); nbins, 180; other
 442 parameters were used as preset in OpenCV. The raw HOG feature comprising 108,391,680 bins
 443 was normalized to 1 to convert a probability histogram. In the comparison between paired two
 444 images, a similarity index was defined as the intersection probability of the HOG features.

445
 446 **Fluorescence Emission Spectrum Transmissive Analysis.** For spectral ratio calculation, data
 447 processing was performed by using the Fiji/ImageJ software (version 2.0.0-rc-49/1.51d)³⁸. All xy
 448 images in raw data (multi-color 3D stack) were smoothed with the median filter (1 pixel). Pixels
 449 having faint or saturated signal values (< 32 or $4063 <$ in 12 bit, respectively) were excluded from
 450 the following calculation. Background area out of beads was detected by an auto-threshold function
 451 with the Otsu method on the Yellow channel and was removed from all channels. Spread bead
 452 cluster images were selected by ROI (region of interest) to exclude the injection trace from the
 453 calculation. The pixels in YG bead clusters were plotted on a scatter graph, corresponding to the
 454 Yellow intensity along the x-axis and the Cyan intensity along the y-axis. At depth of interest,
 455 representative Cyan/Yellow ratio was determined from the slope of the best-fitted regression line
 456 (highest R^2) on the scatter plot, derived from image stacks at its depth $\pm 1.0 \mu\text{m}$. To calculate the
 457 $\Delta\text{Cyan/Yellow}$, the Cyan/Yellow ratio was divided by the average of Cyan/Yellow within the
 458 experimental group at $100 \mu\text{m}$ depth.

459
 460 **Statistics.** All statistical analysis was performed by using R (version 3.3.2)³⁹ with RStudio
 461 software (version 1.0.44). Conventional two-tailed Welch's t -test and Cohen's d were calculated
 462 with the default and the MBESS package (version 4.3.0), respectively. Permuted
 463 Brunner-Munzel⁴¹⁻⁴³ test was executed by the lawstat package (version 3.1) with permutation code.

464 To assess MAGICAL effects on FIDs, we constructed GLMMs with a Gamma error
 465 distribution and a log link function. In the models, fluorescence intensities of pixels (FIPs) were
 466 used as a response variable. The FID of each image stack at the depth $\pm 3 \mu\text{m}$, therefore, was
 467 re-expanded to an intensity list comprised of 786,432 pixels ($512 \times 512 \text{ pixels} \times 3 \text{ sections}$). To
 468 reduce modeling costs, 12,288 pixels (1.56 %) were randomly sampled without overlap from each
 469 list. Saturated pixels (255 in 8 bit) were excluded from modeling due to inaccuracies in
 470 fluorescence intensity. Zero intensity pixels were also excluded to avoid a calculation failure under
 471 the log-link function. “Treatment” (2 levels, MAGICAL or control) and “Depth” (3 levels) were
 472 used as categorical predictor variables with fixed effects. The models included an interaction
 473 between “Treatment” and “Depth.” To overcome pseudo-replications caused by sampling multiple
 474 pixels within each mouse, “Mouse” (26 mice in total) was assigned as a random effect for
 475 intercepts and “Depth” slopes. Thus, the models were described in R as follows:

476 $\text{FIP} \sim \text{Depth} * \text{Treatment} + (\text{Depth} | \text{Mouse})$

477 Consequently, the models comprised 929,331 (CxLV) or 957,264 (HpCA1) pixel observations, in
 478 78 image stacks extracted at 3 depths from 26 mice under 2 treatments.

479 The model fitting was performed via the maximum likelihood according to Laplace
 480 approximation, by using the glmer function in the lme4 package (version 1.1-12). For the estimated
 481 coefficient of fixed effect, Wald-type 95 % confidence interval (CI) was calculated by using the
 482 confint function. The model prediction for each image stack was obtained through the
 483 predict.merMod function in the lme4 package. The fixed effects with asymptotic 95% CI were
 484 estimated by using the Effect function in the effects package (version 3.1-2). Pairwise comparisons
 485 for the predictor variables were examined by the lsmeans function in the lsmeans package (version
 486 2.25-5).

487 As the coefficient of determination for the GLMM, two R^2 statistics are proposed⁴⁴: marginal
 488 and conditional R^2_{GLMM} . The marginal R^2_{GLMM} ($R^2_{GLMM(m)}$) describes the proportion of variance
 489 explained only by fixed effects. The conditional R^2_{GLMM} ($R^2_{GLMM(c)}$) describes the proportion of
 490 variance explained by both fixed and random effects.

491

$$492 \quad R_{GLMM(m)}^2 = \frac{\sigma_{fix}^2}{\sigma_{fix}^2 + \sigma_{random}^2 + \sigma_{residual}^2} \quad (1)$$

$$493 \quad R_{GLMM(c)}^2 = \frac{\sigma_{fix}^2 + \sigma_{random}^2}{\sigma_{fix}^2 + \sigma_{random}^2 + \sigma_{residual}^2} \quad (2)$$

494

495 An original method for the R_{GLMM}^2 was limited only to the GLMM including Poisson or
 496 binomial error distributions and not including random slope terms⁴⁴. However, two extensions had
 497 been individually provided for the R_{GLMM}^2 , to calculate random effects variances in random slope
 498 models⁴⁵ or to evaluate further error distribution in the residual variance⁴⁶. Thus, we calculated the
 499 R_{GLMM}^2 of our models by an R code combining the two extensions as follows: in the extension for
 500 random slope models⁴⁵, provided code generates a square matrix at once but uses only diagonal
 501 elements of the matrix. When the code ran for our models, a large number of observations
 502 generated a huge square matrix, which caused the computation to fail, due to insufficient memory.
 503 Therefore, we calculated only the portion corresponding to the diagonal of the square matrix. On
 504 the other hand, the extension for residual variances was applicable to our models without
 505 modifications. We selected the trigamma function from three candidates in the paper⁴⁶, to evaluate
 506 the models including a Gamma error distribution and a log link function.

507

508 **Data availability.** Data and code are available from the authors upon request.

509

References:

1. Matsuzaki, M., Honkura, N., Ellis-Davies, G. C. R. & Kasai, H. Structural basis of long-term potentiation in single dendritic spines. *Nature* **429**, 761–766 (2004).
2. Chen, X., Leischner, U., Rochefort, N. L., Nelken, I. & Konnerth, A. Functional mapping of single spines in cortical neurons *in vivo*. *Nature* **475**, 501–505 (2011).
3. Trachtenberg, J. T. *et al.* Long-term *in vivo* imaging of experience-dependent synaptic plasticity in adult cortex. *Nature* **420**, 788–794 (2002).
4. Margolis, D. J. *et al.* Reorganization of cortical population activity imaged throughout long-term sensory deprivation. *Nat. Neurosci.* **15**, 1539–1546 (2012).
5. Nemoto, T. Living cell functions and morphology revealed by two-photon microscopy in intact neural and secretory organs. *Mol. Cells* **26**, 113–120 (2008).
6. Ishikawa-Ankerhold, H. C., Ankerhold, R. & Drummen, G. P. C. Advanced fluorescence microscopy techniques—FRAP, FLIP, FLAP, FRET and FLIM. *Molecules* **17**, 4047–4132 (2012).
7. Hama, H. *et al.* Scale: a chemical approach for fluorescence imaging and reconstruction of transparent mouse brain. *Nat. Neurosci.* **14**, 1481–1488 (2011).
8. Ertürk, A. *et al.* Three-dimensional imaging of solvent-cleared organs using 3DISCO. *Nat. Protoc.* **7**, 1983–1995 (2012).
9. Chung, K. *et al.* Structural and molecular interrogation of intact biological systems. *Nature* **497**, 332–337 (2013).
10. Kuwajima, T. *et al.* *Clear^T*: a detergent- and solvent-free clearing method for neuronal and non-neuronal tissue. *Development* **140**, 1364–1368 (2013).
11. Ke, M.-T., Fujimoto, S. & Imai, T. SeeDB: a simple and morphology-preserving optical clearing agent for neuronal circuit reconstruction. *Nat. Neurosci.* **16**, 1154–1161 (2013).
12. Susaki, E. A. *et al.* Whole-brain imaging with single-cell resolution using chemical cocktails and computational analysis. *Cell* **157**, 726–739 (2014).

13. Aoyagi, Y., Kawakami, R., Osanai, H., Hibi, T. & Nemoto, T. A rapid optical clearing protocol using 2,2'-thiodiethanol for microscopic observation of fixed mouse brain. *PLoS ONE* **10**, e0116280 (2015).
14. Holtmaat, A. *et al.* Long-term, high-resolution imaging in the mouse neocortex through a chronic cranial window. *Nat. Protoc.* **4**, 1128–1144 (2009).
15. Frank, M. S. B., Nahata, M. C. & Hilty, M. D. Glycerol: a review of its pharmacology, pharmacokinetics, adverse reactions, and clinical use. *Pharmacotherapy* **1**, 147–160 (1981).
16. Cantore, G., Guidetti, B. & Virno, M. Oral glycerol for the reduction of intracranial pressure. *J. Neurosurg.* **21**, 278–283 (1964).
17. Meyer, J. S., Charney, J. Z., Rivera, V. M. & Mathew, N. T. Treatment with glycerol of cerebral oedema due to acute cerebral infarction. *Lancet* **298**, 993–997 (1971).
18. Mathew, N. T., Rivera, V. M., Meyer, J. S., Charney, J. Z. & Hartmann, A. Double-blind evaluation of glycerol therapy in acute cerebral infarction. *Lancet* **300**, 1327–1329 (1972).
19. Meyer, J. S. *et al.* Circulatory and metabolic effects of glycerol infusion in patients with recent cerebral infarction. *Circulation* **51**, 701–712 (1975).
20. Wald, S. L. & McLaurin, R. L. Oral glycerol for the treatment of traumatic intracranial hypertension. *J. Neurosurg.* **56**, 323–331 (1982).
21. Berger, C., Sakowitz, O. W., Kiening, K. L. & Schwab, S. Neurochemical monitoring of glycerol therapy in patients with ischemic brain edema. *Stroke* **36**, e4–e6 (2005).
22. Sloviter, H. A., Shimkin, P. & Suhara, K. Glycerol as a substrate for brain metabolism. *Nature* **210**, 1334–1336 (1966).
23. Kawakami, R. *et al.* Visualizing hippocampal neurons with *in vivo* two-photon microscopy using a 1030 nm picosecond pulse laser. *Sci. Rep.* **3**, 1014 (2013).
24. Kawakami, R. *et al.* *In vivo* two-photon imaging of mouse hippocampal neurons in dentate gyrus using a light source based on a high-peak power gain-switched laser diode. *Biomed. Opt. Express* **6**, 891–901 (2015).

25. Pérez-Alvarez, A., Araque, A. & Martin, E. D. Confocal microscopy for astrocyte *in vivo* imaging: recycle and reuse in microscopy. *Front. Cell. Neurosci.* **7**, 51 (2013).
26. Wen, X., Mao, Z., Han, Z., Tuchin, V. V. & Zhu, D. *In vivo* skin optical clearing by glycerol solutions: mechanism. *J Biophoton.* **3**, 44–52 (2010).
27. Zhao, Y.-J. *et al.* Skull optical clearing window for *in vivo* imaging of the mouse cortex at synaptic resolution. *Light Sci Appl* **7**, 17153 (2018).
28. Cameron, G. R. & Finckh, E. S. The production of an acute haemolytic crisis by the subcutaneous injection of glycerol. *J. Pathol. Bacteriol.* **71**, 165–172 (1956).
29. Kimelberg, H. K. Current concepts of brain edema - review of laboratory investigations. *J. Neurosurg.* **83**, 1051–1059 (1995).
30. Kawauchi, S. *et al.* Simultaneous measurement of changes in light absorption due to the reduction of cytochrome c oxidase and light scattering in rat brains during loss of tissue viability. *Appl. Opt.* **47**, 4164–4176 (2008).
31. Kawauchi, S. *et al.* Light-scattering signal may indicate critical time zone to rescue brain tissue after hypoxia. *J. Biomed. Opt.* **16**, 027002 (2011).
32. Johnson, V., Carlson, A. J. & Johnson, A. Studies on the physiological action of glycerol on the animal organism. *Am. J. Physiol.* **103**, 517–534 (1933).
33. Hine, C. H., Anderson, H. H., Moon, H. D., Dunlap, M. K. & Morse, M. S. Comparative toxicity of synthetic and natural glycerin. *A.M.A. Arch. Ind. Hyg. Occup. Med.* **7**, 282–291 (1953).
34. Awasthi, P. & Srivastava, S. N. Role of oral glycerol in glaucoma. *Br. J. Ophthalmol.* **49**, 660–666 (1965).
35. Klar, T. A., Jakobs, S., Dyba, M., Egner, A. & Hell, S. W. Fluorescence microscopy with diffraction resolution barrier broken by stimulated emission. *Proc. Natl. Acad. Sci. U.S.A.* **97**, 8206–8210 (2000).

36. Noguchi, J. *et al.* *In vivo* two-photon uncaging of glutamate revealing the structure-function relationships of dendritic spines in the neocortex of adult mice. *J. Physiol. (Lond.)* **589**, 2447–2457 (2011).
37. Livet, J. *et al.* Transgenic strategies for combinatorial expression of fluorescent proteins in the nervous system. *Nature* **450**, 56–62 (2007).
38. Schindelin, J. *et al.* Fiji: an open-source platform for biological-image analysis. *Nat Methods* **9**, 676–682 (2012).
39. R Core Team. R: a language and environment for statistical computing. (2016). Available at: <https://www.r-project.org/>
40. Dalal, N. & Triggs, B. Histograms of oriented gradients for human detection. *2005 IEEE Comput. Soc. Conf. Comput. Vis. Pattern Recognit. (CVPR'05)* **1**, 886–893 (2005). doi: 10.1109/CVPR.2005.177
41. Brunner, E. & Munzel, U. The nonparametric Behrens–Fisher problem: asymptotic theory and a small–sample approximation. *Biom. J.* **42**, 17–25 (2000).
42. Neubert, K. & Brunner, E. A studentized permutation test for the non-parametric Behrens–Fisher problem. *Comput. Stat. Data Anal.* **51**, 5192–5204 (2007).
43. Neuhäuser, M. & Ruxton, G. D. Distribution-free two-sample comparisons in the case of heterogeneous variances. *Behav Ecol Sociobiol* **63**, 617–623 (2009).
44. Nakagawa, S. & Schielzeth, H. A general and simple method for obtaining R^2 from generalized linear mixed-effects models. *Methods Ecol. Evol.* **4**, 133–142 (2013).
45. Johnson, P. C. D. Extension of Nakagawa & Schielzeth's R^2_{GLMM} to random slopes models. *Methods Ecol. Evol.* **5**, 944–946 (2014).
46. Nakagawa, S. & Schielzeth, H. Coefficient of determination R^2 and intra-class correlation coefficient ICC from generalized linear mixed-effects models revisited and expanded. *bioRxiv* 095851 (2016). doi:10.1101/095851

615 **Endnotes:**

616

617 **Acknowledgments** We thank Nikon Imaging Center (NIC) at Hokkaido University for technical
 618 support with a 60× objective lens. This research was supported by the “Brain/MIND” from the
 619 Japan Agency for Medical Research and Development (AMED); by the MEXT/JSPS KAKENHI
 620 Grant Number JP15H05953 “Resonance Bio” from the Japan Society for the Promotion of
 621 Sciences (JSPS) in the Ministry of Education, Culture, Sports, Science and Technology (MEXT);
 622 by the “Network Joint Research Center for Materials and Devices” in the MEXT and by the
 623 “Dynamic Alliance for Open Innovation Bridging Human, Environment and Materials” in the
 624 MEXT.

625

626 **Author Contributions** K.I., R.K., and T.N. designed the research. K.I. and T.O. performed
 627 experiments and analyzed the data. K.I. and T.N. wrote the paper.

628

629 **Additional Information** The authors declare no conflicts of interest related to this research.
 630 Correspondence and requests for materials should be addressed to T.N. (tn@es.hokudai.ac.jp).

631

Figures and Figure Legends:

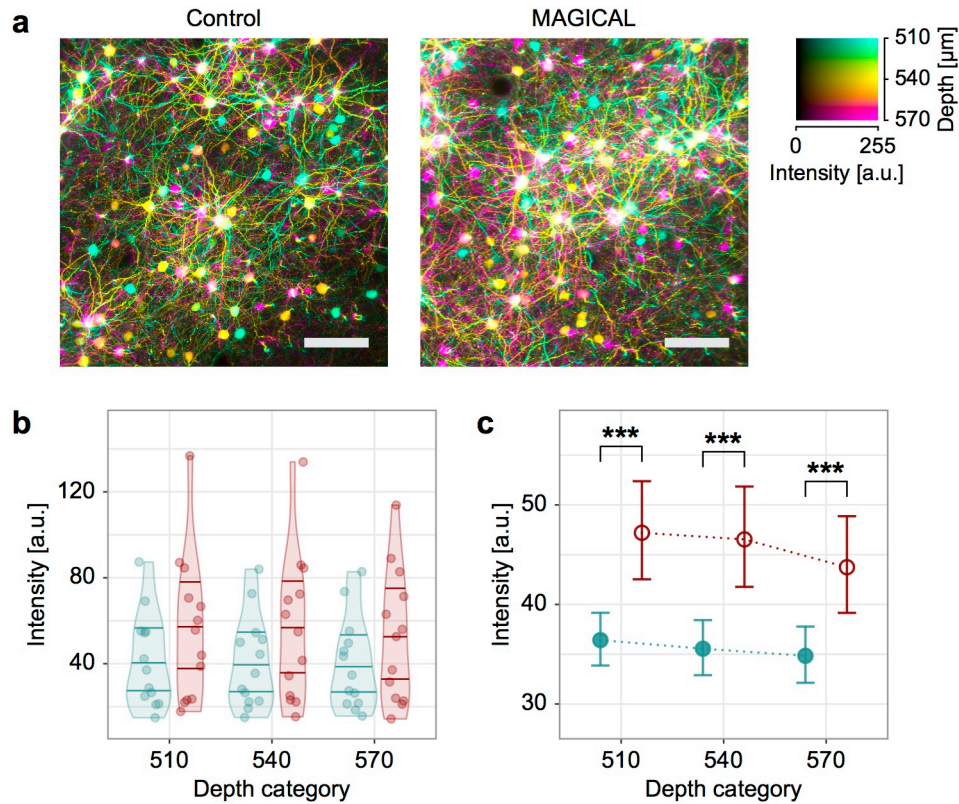


Fig 1. *In vivo* two-photon imaging at CxLV. (a) DccMIP images of CxLV at $540 \pm 30 \mu\text{m}$ depth in control and MAGICAL. scale bar $100 \mu\text{m}$. (b–c) Representative fluorescence intensity, predicted by the GLMM for each image stack (b) and “Treatment” group (c), along “Depth.” Distribution of plots in (b) is visualized with violin plots estimated by Gaussian kernel and with 0.25, 0.50, and 0.75 quantile lines. Error bars in (c) are asymptotic 95 % CI. Red, MAGICAL; Blue, control; *** $p < 0.001$; a.u., arbitrary unit.

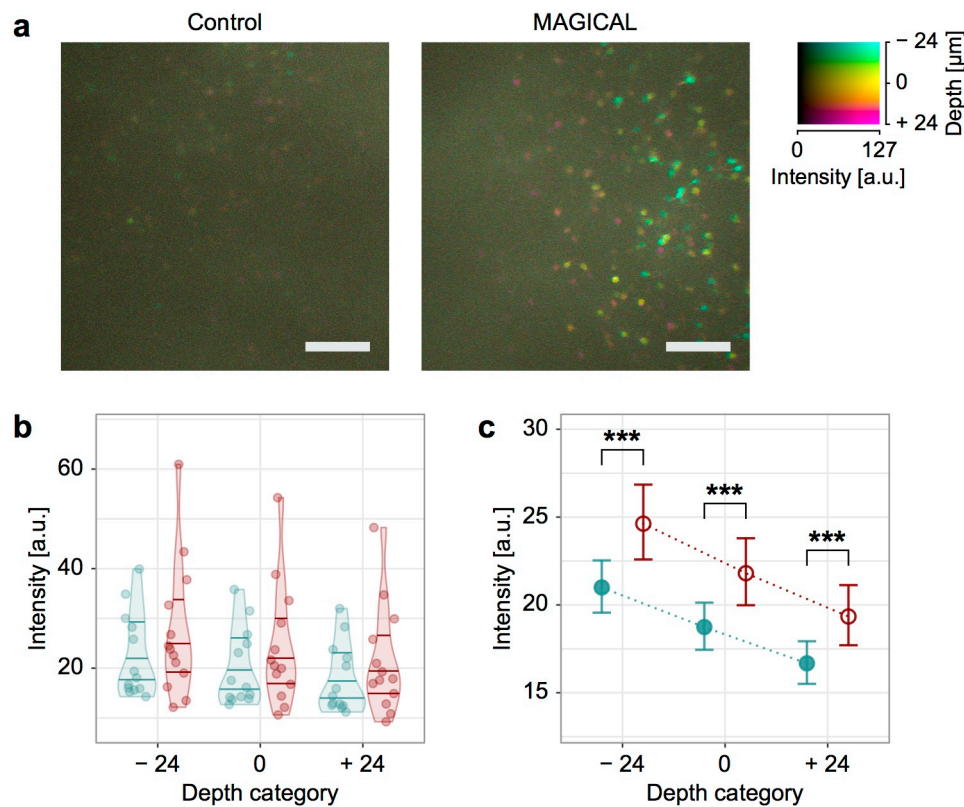
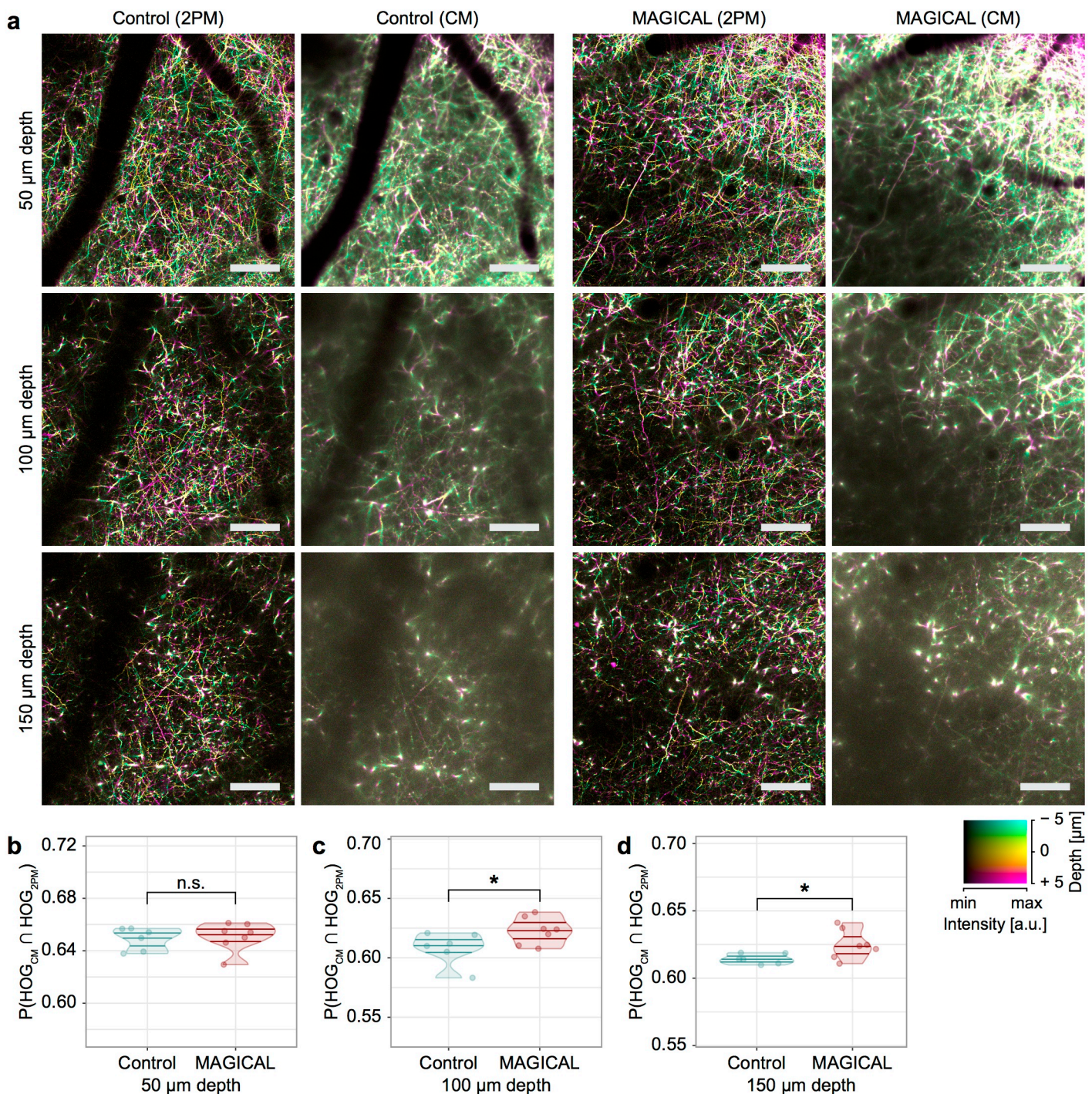


Fig 2. *In vivo* two-photon imaging at HpCA1. (a) DccMIP images of HpCA1 approximately at 975 ± 24 μm depth in control and MAGICAL. In the color code, each center depth is shown as 0 μm relative depth. scale bar 100 μm. (b–c) Representative fluorescence intensity, predicted by the GLMM for each image stack (b) and “Treatment” group (c), along “Depth.” Distribution of plots in (b) is visualized with violin plots estimated by Gaussian kernel and with 0.25, 0.50, and 0.75 quantile lines. Error bars in (c) are asymptotic 95 % CI. Red, MAGICAL; Blue, control; *** $p < 0.001$; a.u., arbitrary unit.

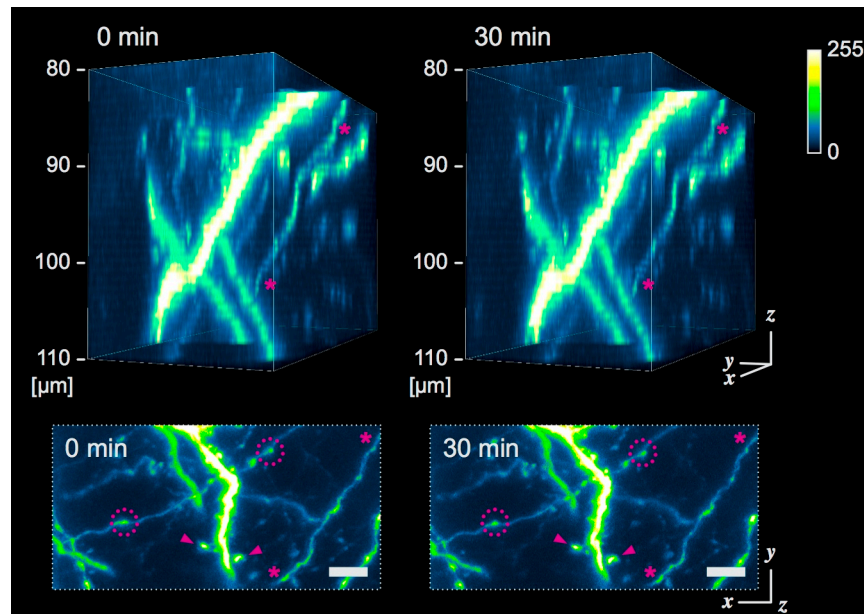


650

651 **Fig 3. *In vivo* confocal imaging at CxLI.** (a) DccMIP images of CxLI at $50 \pm 5 \mu\text{m}$, $100 \pm 5 \mu\text{m}$,
652 and $150 \pm 5 \mu\text{m}$ depth, by using two-photon microscopy (2PM) and confocal microscopy (CM).
653 The display range of fluorescence intensity (min–max in 8 bits) is adjusted as follow: 2PM images
654 at every depth, (0–127); CM images at 50, 100, and 150 μm depth, (0–255), (0–127), and (0–63),
655 respectively. In the color code, each center depth is shown as 0 μm relative depth. scale bar 100 μm .
656 (b–d) Similarities of the DccMIP images between CM and 2PM at $50 \pm 5 \mu\text{m}$ (b), $100 \pm 5 \mu\text{m}$ (c),

657 and $150 \pm 5 \mu\text{m}$ (**d**) depth. $P(\text{HOG}_{\text{CM}} \cap \text{HOG}_{2\text{PM}})$, probability of intersection between HOG
658 features extracted from the CM image and the 2PM image; $n = 6$ mice in control and $n = 7$ mice in
659 MAGICAL; n.s., not significant; * $p < 0.05$; a.u., arbitrary unit.

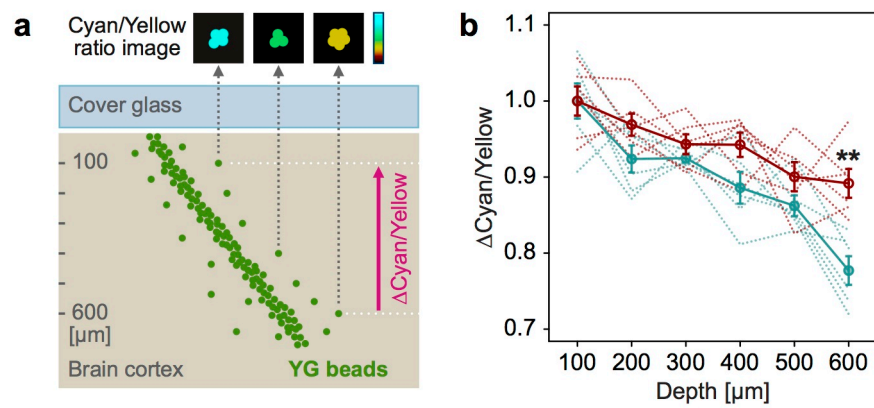
660



661

662 **Fig 4. *In vivo* confocal high-resolution 4D imaging.** Fine confocal 3D images with MAGICAL,
663 captured with time lapse at 5-min intervals for 30 min. 3D images (upper) were reconstructed from
664 31 optical sections at 1 $\mu\text{m}/\text{step}$. A fine fiber (asterisk) was visualized with less optical aberration
665 along the z-axis. In maximum intensity projection (MIP) images (bottom), synaptic structures, such
666 as dendritic spines (arrow-head) and axonal boutons (dotted circle) were observable. Despite a
667 totality of 217 scans, remarkable bleaching and phototoxic effects were not observed. scale bar 5
668 μm .

669



670

671 **Fig 5. Optical evaluation for living brains.** (a) Schematic illustration of the FESTA by using
672 fluorescent YG bead clusters injected into living brains. (b) *In vivo* spectral transmission ratio
673 (Δ Cyan/Yellow) while the light returned from deeper regions to 100 μ m depth. Red, MAGICAL;
674 Blue, control; Solid line, average with standard error; Dotted line, each trial; $n = 6$ mice in each
675 group; ** $p < 0.01$.

676